J Mol Model (2014) 20:2505
DOI 10.1007/s00894-014-2505-0

ORIGINAL PAPER

Molecular dynamics simulations of the mechanical properties of monoclinic hydroxyapatite

Xiang Ou · Qiang Han

Received: 16 June 2014 / Accepted: 13 October 2014 / Published online: 30 October 2014
© Springer-Verlag Berlin Heidelberg 2014

Abstract Inorganic biomedical materials are of great interest in the biomedical field. One such material, hydroxyapatite (HAP), is the main inorganic substance in the hard tissue of bones and teeth in the human body. Until recently, studies of the mechanical properties of HAP by uniaxial tension testing and compression molecular dynamics (MD) simulation had remained difficult. In addition, electric charges used in such simulations alter the molecular structure of HAP. Here, we present the mechanical properties and new charges of the monoclinic form of HAP using the self-consistent charge equilibration (QEq) scheme proposed by Rappé and Goddard in 1991 (J Phys Chem 95:3358–3363), and a successful MD simulation of the uniaxially tensile and compressive properties of monoclinic HAP. Also presented is the change in potential energy in the cell and how temperature and strain rate affect the uniaxial tension and compressive properties of HAP. Additionally, we compare the mechanical properties of this substance along different directions, and some conclusions useful for further studies of the mechanical properties of HAP composite materials are discussed.

Keywords Monoclinic hydroxyapatite · Uniaxial tension · Uniaxial compression · QEq charge equilibration method · Strain rate

Electronic supplementary material The online version of this article (doi:10.1007/s00894-014-2505-0) contains supplementary material, which is available to authorized users.

X. Ou · Q. Han (✉)
School of Civil Engineering and Transportation,
South Chian University of Technology,
Guangzhou, Guangdong, People's Republic of China
e-mail: emqhan@scut.edu.cn
URL: http://www.scut.edu.cn

X. Ou
e-mail: scut_ouxiang@163.com

Introduction

Hydroxyapatite (HAP)—a calcium phosphate bioceramic mineral with anisotropy [1]—consists of Ca^{2+}, PO_4^{3-}, OH^-, and crystallizes in either monoclinic or hexagonal symmetry. When HAP crystallizes in hexagonal symmetry, it has anisotropy in the *z*- (0001) direction, and isotropy in the *x*-, and *y*- (1010) directions [2–5]. However, when it crystallizes in monoclinic symmetry, it has anisotropy in *x*-, *y*-, *z*- directions, and its chemical formula is Ca5(PO4)3OH [6]. The space group of its unit cell is P21/B. The lattice parameters are a=9.4214 Å, b=2a, c=6.8814 Å, $\alpha=\beta=90°$, $\gamma=120°$. In this work, we studied the mechanical properties of monoclinic HAP.

HAP is the main inorganic substance in the hard tissue of bones and teeth in the human body. Its ratios in bones and teeth are 77 % and 97 %, respectively. HAP also has excellent surface properties and biocompatibility [7, 8]. Therefore, HAP is considered the best potential alternate material for biomedical implants involving the hard tissue of bones and teeth in the human body. However, the strength and tenacity of pure HAP are low [9, 10], so HAP can be used only in small implants.

In the recent years, research on HAP has focused mainly on the following three aspects:

First is research into developing compact HAP into porous HAP [9]. Compact HAP has excellent mechanical properties, but sclerotin can be formed on the surface of HAP only after it is implanted into the body. Therefore, compact HAP cannot make bone grow effectively. Porous HAP can make both hard and soft tissue grow into HAP itself and thus boost the growth of bone. However, the strength of porous HAP is low and it can be used only in small implants.

Second is research on using HAP as a surface coating material [10]. When HAP is used as a surface coating material on a metal implant, it not only provides a favorable biocompatible

environment and maintains a stable structure for repair and growth of the bone, but also prevents the metal ion from spreading into the human body and keeps the metal away from the corrosive effects of bodily fluids.

Third is research into HAP as a composite material [11]. The mechanical properties of pure HAP are usually not strong enough for current requirements in the field of biomedicine. As a result, researchers have attempted to make HAP composite materials in order to improve its mechanical properties.

However, measuring the uniaxial tension and performing compression molecular dynamics (MD) simulation of HAP has, until recently, still been difficult. The reason for this is that it is difficult to keep HAP free in the vertical direction of tension or compression. In addition, electric charges used in such simulations will change the molecular structure of HAP. Yaghmaei et al. [12] reported MD simulation of the stress–strain properties of a nanocomposite made from HAP, a single-walled carbon nanotube, and a double-walled carbon nanotube, based on the consistent-valence forcefield (CVFF). They found a significant change in the yield strain of the reinforced nanocomposite, while there was no enhancement of the magnitude of the Young modulus of the reinforced HAP, vis-a-vis pure HAP. However, when modeling HAP through MD simulation, the electric charges [13] used resulted in an abnormal shape of the phosphate group in HAP, and made the locations of the atoms of HAP stray significantly from their correct locations.

The present study investigated the mechanical properties of monoclinic HAP. Here, we present new charges of monoclinic HAP determined via the self-consistent charge equilibration (QEq) scheme, which make the location of the atoms in HAP consistent with their actual location. The QEq method, proposed by Rappé and Goddard [14], implements a variable-charge model by requiring the chemical potential at each atom to be equivalent, and this requirement for equal chemical potential leads to equilibrium charges that depend on geometry. In addition, HAP was modeled in Materials Studio (http://accelrys.com/products/materials-studio/), based on the polymer consistent forcefield (PCFF) [15–18], which was developed based on CFF91 (one of the consistent forcefields) and is intended for application to organic and inorganic materials. We successfully performed MD simulation of the uniaxially tensile and compressive properties of monoclinic HAP in Lammps (http://lammps.sandia.gov/). Next, we studied the change in potential energy in the cell and how temperature and the strain rate affect the uniaxial

Table 1 Atomic fractional coordinates in a monoclinic hydroxyapatite (HAP) unit cell. *MD* Molecular dynamics

Atom	*x*		*y*		*z*	
	Document 1 coordinate	MD coordinate	Document 1 coordinate	MD coordinate	Document 1 coordinate	MD coordinate
OIA	0.3286(3)	0.3073(3)	0.4918(2)	0.4863(5)	0.2604(5)	0.2767(9)
OIIA	0.5866(3)	0.5914(6)	0.4828(2)	0.4929(9)	0.2365(5)	0.2645(1)
OIIIA	0.3280(4)	0.3478(9)	0.3746(2)	0.3808(4)	0.0821(4)	0.0776(1)
OIVA	0.3578(3)	0.3543(7)	0.3827(1)	0.3750(5)	0.4404(3)	0.4443(8)
PA	0.3982(1)	0.3994(0)	0.4342(0)	0.4349(6)	0.2556(2)	0.2664(0)
OIB	0.4850(2)	0.4794(5)	0.3282(1)	0.3308(7)	0.7604(5)	0.7771(2)
OIIB	0.5359(2)	0.5280(6)	0.3105(1)	0.3085(4)	0.2422(5)	0.2222(6)
OIIIB	0.7473(4)	0.7597(1)	0.2904(2)	0.2867(5)	0.0804(4)	0.0866(9)
OIVB	0.7373(4)	0.7348(9)	0.2949(2)	0.3024(0)	0.4390(4)	0.4479(2)
PB	0.6315(1)	0.6331(6)	0.2650(0)	0.2656(2)	0.2552(2)	0.2572(7)
OIC	0.1568(2)	0.1671(9)	0.5858(1)	0.5902(2)	0.2462(5)	0.2222(2)
OIIC	0.1213(3)	0.1231(8)	0.5438(1)	0.5357(1)	0.7319(4)	0.7069(4)
OIIIC	0.0794(3)	0.0556(0)	0.4134(2)	0.3883(9)	0.5817(3)	0.6035(8)
OIVC	0.0909(4)	0.0955(0)	0.4290(2)	0.4293(8)	0.9397(4)	0.9548(8)
PC	0.0302(1)	0.0236(1)	0.4490(0)	0.4413(5)	0.7518(2)	0.7599(4)
OH	−0.0007(3)	0.0031(7)	0.2504(2)	0.2570(7)	0.3045(3)	0.3478(5)
H	0	0.0190(4)	0.2500	0.2662(2)	0.4392	0.4873(7)
Ca I	0.3259(1)	0.3329(6)	0.5798(1)	0.5712(8)	0.0006(1)	−0.0116(3)
Ca II	0.3412(1)	0.3559(4)	0.5868(1)	0.5954(3)	0.4977(1)	0.4949(8)
Ca III	0.2465(1)	0.2292(9)	0.2465(0)	0.2426(5)	0.2534(1)	0.2537(2)
Ca IV	−0.0068(1)	−0.0073(7)	0.6233(0)	0.6190(7)	0.7434(1)	0.7311(9)
Ca V	0.2533(1)	0.2438(7)	0.3732(0)	0.3594(0)	0.7567(1)	0.7596(4)

tension and compressive properties of HAP. Additionally, we also compared the tensile and compressive properties of HAP respectively along the *x*-, *y*- and *z*- directions. As a result, some conclusions useful for the study of mechanical properties of HAP composite material could be made.

Details of modeling monoclinic HAP

The chemical formula of monoclinic HAP is Ca5(PO4)3OH. The space group of its unit cell is *P*21/B. The lattice parameters are $a=b=9.4214$ Å, $c=6.8814$ Å, $\alpha=\beta=90°$, $\gamma=120°$. The fractional coordinates of all atoms in a HAP unit cell are shown in Table 1.

After modeling HAP in Materials Studio (http://accelrys.com/products/materials-studio/) with lattice parameters and the atomic fractional coordinates shown in Table 1, the charges of atoms were calculated by the QEq charge equilibration method [14]. The results obtained are shown in Table 2. A geometry optimization of the HAP unit cell was performed and the atomic fractional coordinates shown in Table 1 were found.

The unit cell of HAP after geometry optimization is shown in Fig. 1. From Fig. 1 and the atomic fractional coordinates shown in Table 1, we can easily see that the new charges calculated using the QEq charge equilibration method make the location of the atoms in HAP consistent with their actual location, and that the phosphate group keeps its normal shape.

A super cell of pure HAP (Fig. 2 ; 7, 3, and 5 unit cells respectively in the *x*-, *y*- and *z*-directions) was made by stacking the unit cells. The super cell consisted of 105 unit cells totaling 2,310 atoms. The force field parameters to the super cell were then given based on the PCFF force field using the electric charges shown in Table 2. Terms included in the PCFF forcefield are given in Eq. 1. Lines 1 and 2 describes bond stretching and angle bending, respectively. Line 3 describes torsions with a three-term Fourier. Line 4 defines the out-of-plane coordinates. Significant cross-terms up to third order (Lines 5–11) are also included. The Coulombic interactions between the atomic charges are represented by Line 12. Line 13 characterizes the Van der Waals interactions [15–18].

Table 2 New charges calculated by the QEq charge equilibration method [14].

Atom	Charge	Atom	Charge	Atom	Charge
OIA	−0.586734	OIC	−0.588013	Ca IV	+1.21611
OIIA	−0.569151	OIIC	−0.568870	Ca V	+1.21646
OIIIA	−0.592624	OIIIC	−0.592638		
OIVA	−0.585048	OIVC	−0.586422		
PA	+0.479527	PC	+0.478796		
OIB	−0.587686	OH	−0.865292		
OIIB	−0.567817	H	0.265721		
OIIIB	−0.597530	Ca I	+1.25490		
OIVB	−0.576096	Ca II	+1.25430		
PB	+0.480976	Ca III	+1.21713		

$$
\begin{aligned}
E_{pot} &= \sum_{b}\left[K_2(b-b_0)^2+K_3(b-b_0)^3+K_4(b-b_0)^4\right]\\
&+\sum_{\theta}\left[H_2(\theta-\theta_0)^2+H_3(\theta-\theta_0)^3+H_4(\theta-\theta_0)^4\right]\\
&+\sum_{\phi}\left[V_1\left[1-\cos\left(\phi-\phi_1^0\right)\right]+V_2\left[1-\cos\left(2\phi-\phi_2^0\right)\right]+V_3\left[1-\cos\left(3\phi-\phi_3^0\right)\right]\right]\\
&+\sum_{\chi}K_\chi\chi^2\\
&+\sum_{b}\sum_{b'}F_{bb'}(b-b_0)(b'-b_0')\\
&+\sum_{\theta}\sum_{\theta'}F_{\theta\theta'}(\theta-\theta_0)(\theta'-\theta_0')\\
&+\sum_{b}\sum_{\theta}F_{b\theta}(b-b_0)(\theta-\theta_0)\\
&+\sum_{b}\sum_{\phi}(b-b_0)[V_1\cos\phi+V_2\cos2\phi+V_3\cos3\phi]\\
&+\sum_{b'}\sum_{\phi}(b-b_0)[V_1\cos\phi+V_2\cos2\phi+V_3\cos3\phi]\\
&+\sum_{\theta}\sum_{\phi}(\theta-\theta_0)[V_1\cos\phi+V_2\cos2\phi+V_3\cos3\phi]\\
&+\sum_{\phi}\sum_{\theta}\sum_{\theta'}K_{\phi\theta\theta'}\cos\phi(\theta-\theta_0)(\theta'-\theta_0')\\
&+\sum_{i>j}\frac{q_iq_j}{\varepsilon r_{ij}}\\
&+\sum_{i>j}\left[\frac{A_{ij}}{r_{ij}^9}-\frac{B_{ij}}{r_{ij}^6}\right]
\end{aligned}
\tag{1}
$$

MD simulation of the uniaxially tensile and compressive properties of monoclinic HAP was performed in Lammps (http://lammps.sandia.gov/). The timestep was 1 fs. During the simulation, if the HAP was stretched (or compressed) along one direction (*x*-, *y*-, or *z*-), the pressure in the other two orthogonal directions was controlled to be zero. For example, the pressure in the *x*-, *y*- directions was controlled to zero when the HAP was stretched (or compressed) along the *z*- direction. The ensemble used was NPT, which means the simulations were performed on systems with a fixed number of atoms, a barostat was used to control the pressure, and a thermostat controlled the temperature. The force field remained PCFF. The temperatures were maintained at 200 K, 300 K, 400 K, 500 K, respectively, via a Nose-Hoover thermostat and the strain rates chosen were 1.0×10^{10}/s, 5.0×10^{10}/s, and 1.0×10^{11}/s.

The period boundary conditions were applied in the *x*-, *y*-, and *z*- directions. Before the uniaxial tension and compression MD simulation, pure HAP was equilibrated at 500 K for 50 ps, and then equilibrated from 500 K to the target temperature for 50 ps, and finally equilibrated at the target temperature for 50 ps. If the target temperature was 500 K, the pure

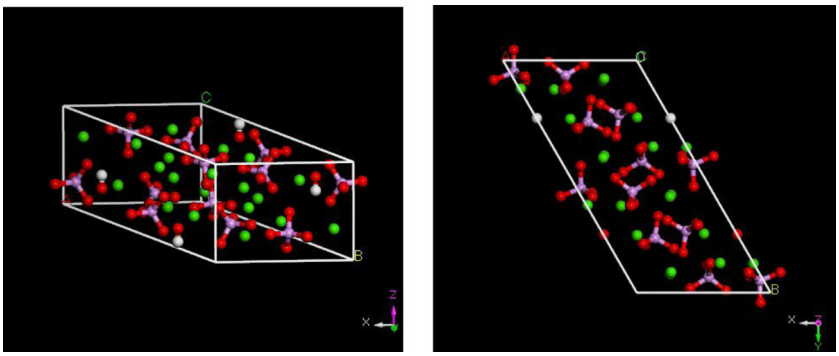

(a) 3D view of HAP unit cell (b) Top view of HAP unti cell

Fig. 1 Hydroxyapatite (HAP) unit cell modeled with charges shown in Table 2

HAP was stretched (or compressed) directly after the equilibration at 500 K for 50 ps. During the uniaxial tension and compression MD simulation, pure HAP was stretched (or compressed) $\Delta\varepsilon$ every femtosecond in the *x*-, *y*- or *z*-direction, and the $\Delta\varepsilon$ was determined by the strain rate. The cutoff was set to 12.5 Å. In addition, the temperatures we chose were not 0 K; as a result, all the variations obtained were of the sawtooth type. This is normal in MD simulation.

Results and discussion

Uniaxial tension and compression

Figure 3a, b illustrates the stress–strain variations in the case of uniaxially tensile and compressive strain applied along the *x*-direction. We can clearly see that stress in the *z*-direction varies with the strain; however, stress in the *y*- and *z*-directions fluctuates near zero. This is the uniaxial tension and uniaxial compression. Figure 3c, d and Fig. 3e, f show the stress–strain variations in the case of uniaxially tensile and compressive strain applied along the *y*- and *z*-direction, respectively. It is obvious that the stress in the tensile and compressive direction varies with the strain; however, stress in the other two directions perpendicular to the forced direction fluctuates near zero. This is also the uniaxial tension and uniaxial compression.

Tension

Tables 3, 4 and 5 show the tensile fracture strength, fracture strain and Young's modulus of HAP along *x*-, *y*-, *z*- direction, respectively, in different strain rates and temperatures.

Figure 4 shows the stress–strain variations for the case of uniaxially tensile strain applied along the *x*-, *y*-, *z*-direction, respectively, at the same strain rate, but at different temperatures.

Figure 5 shows the stress–strain variations for the case of uniaxially tensile strain applied along the *x*-, *y*-, *z*- direction, respectively, at the same temperature, but at different strain rates.

From Figs. 4 and 5 and Tables 3–5, the tensile fracture strength and Young's modulus of HAP is seen to decrease with a rise in temperature at the same strain rate, but the drop in fracture strength is small. Moreover, the tensile fracture strength and Young's modulus of HAP clearly went up significantly with the rise in strain rate at the same temperature. However, both strain rate and temperature have almost no impact on the tensile fracture strain of HAP. Therefore, the strain rate has more impact than temperature on both Young's modulus and fracture strength of HAP.

On the other hand, in Yaghmaei's [12] study, when pure HAP was stretched along the *z*-direction at a temperature of 300 K and a strain rate of 1.47×10^{10}/s, the Young's modulus

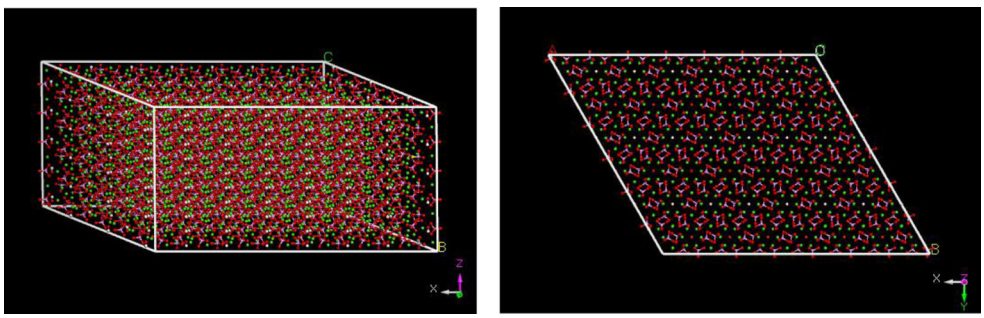

(a) 3Dview (b) Top view

Fig. 2 Super cell of pure HAP

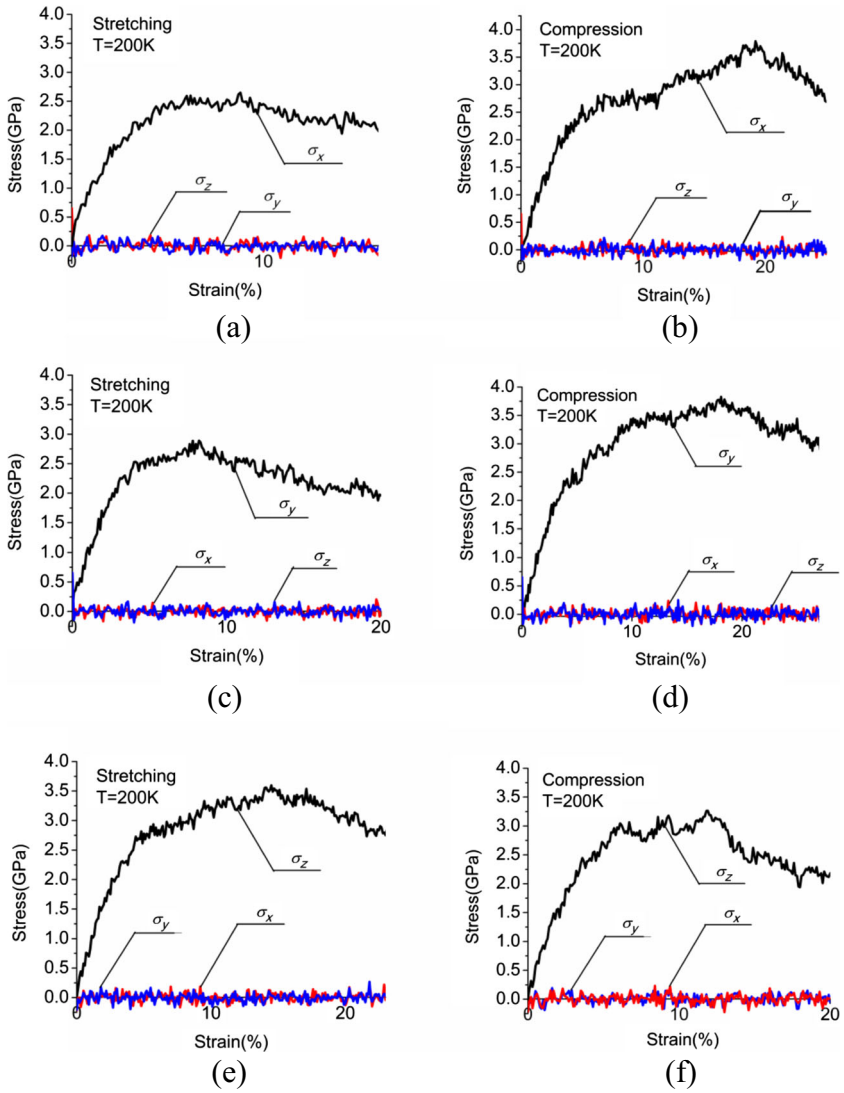

Fig. 3a–f Stress–strain variations for the case of uniaxially tensile and compressive strain respectively applied along the *z*-, *x*-, *y*- direction under the strain rate of 1.0×10^{10}/s. **a**, **b** *x*-direction; **c**, **d** *y*-direction; **e**, **f** *z*-direction

was 55.5 GPa. When it was stretched along the y- direction at the same temperature and a strain rate of 1.027×10^{10}/s, the Young's modulus was 59.19 GPa. However, in our study, at the same temperature of 300 K and a similar but lower strain rate of 1.0×10^{10}/s, the Young's modulus was 64.785 Gpa (higher than 55.05 GPa) in the *z*-direction, and 64.024 GPa (higher than 59.19 GPa) in the *y*-direction. The reason for the difference is simply the veracity of the HAP model. When modeling HAP through MD simulation, the electric charges used by Yaghmaei [13] resulted in an abnormal shape of the phosphate group in HAP, and made the locations of the atoms of HAP stray significantly from their correct locations. Table 1 and Fig. 1 clearly show that the new charges calculated by the QEq charge equilibration method make the location of HAP atoms consistent with their actual location, and the phosphate group maintains its normal shape. This will help build a more precise model of HAP.

In addition, from Tables 3–5, and Fig. 6, we find that when HAP was stretched along different directions at the same temperature and strain rate, the tensile fracture strength along the *z*-direction was always much higher than that along the *x*- and *y*-directions, and the tensile fracture strength along the *y*-direction was a little bit higher than that along the *x*-direction. It can therefore be concluded that the tensile property of HAP in the *z*-direction is much better than that along the *x*-, and *y*-directions, and the tensile property along the *y*-direction is a little better than that along the *x*-direction. However, the tensile Young's modulus of HAP along the *z*-direction is always lower than that along *x*- and *y*-direction at the same temperature and strain rate.

Figure 7 shows the change in potential energy of HAP under tension at 300 K and a strain rate of 1.0×10^{10}/s. From Figs. 7a and 8b, it is clear that the bond energy decreases with the rise in strain, but the variation in the amplitude of the angle energy is very small. As a result, the change in molecular

Table 3 Tensile fracture strength, fracture strain and Young's modulus of HAP along the *x*-direction at different strain rates and temperatures

Temperature (K)	Fracture strength (GPa)	Fracture strain (GPa)	Young's modulus (GPa)
	Strain rate 1.0×10^{10}/s		
200	2.649	0.088	83.212
300	2.327	0.077	79.013
400	1.992	0.071	76.352
500	1.464	0.067	50.822
	Strain rate 5.0×10^{10}/s		
200	3.293	0.067	93.772
300	3.150	0.079	87.540
400	2.712	0.076	77.775
500	2.288	0.098	58.927
	Strain rate 1.0×10^{11}/s		
200	3.788	0.076	135.687
300	3.527	0.082	122.727
400	3.417	0.066	108.538
500	2.651	0.105	87.755

energy (molecular energy=angle energy+bond energy) of HAP is caused mainly by the bond energy. From Fig. 7c, d, it can be seen that the variation in amplitude of the Van der Waals pairwise energy is very small compared with the Coulombic pairwise energy. Therefore, during the tension, the change in pair energy (pair energy=Van der Waals pairwise energy+Coulombic pairwise energy) in pure HAP is caused mainly by the change in Coulombic pairwise energy.

Table 4 Tensile fracture strength, fracture strain and Young's modulus of HAP along the *y*-direction at different strain rates and temperatures

Temperature(K)	Fracture strength (GPa)	Fracture strain (GPa)	Young's modulus (GPa)
	Strain rate 1.0×10^{10}/s		
200	2.890	0.082	75.564
300	2.457	0.057	64.024
400	2.229	0.048	57.570
500	1.464	0.074	44.883
	Strain rate 5.0×10^{10}/s		
200	3.542	0.083	107.792
300	3.153	0.076	85.546
400	2.951	0.085	81.806
500	2.611	0.077	79.655
	Strain rate 1.0×10^{11}/s		
200	4.080	0.083	119.784
300	3.812	0.094	118.297
400	3.471	0.079	100.904
500	3.155	0.088	94.829

Table 5 Tensile fracture strength, fracture strain and Young's modulus of HAP along the *z*- direction at different strain rates and temperatures

Temperature(K)	Fracture strength (GPa)	Fracture strain (GPa)	Young's modulus (GPa)
	Strain rate 1.0×10^{10}/s		
200	3.596	0.145	70.122
300	3.007	0.125	64.785
400	2.870	0.162	55.952
500	2.722	0.155	35.795
	Strain rate 5.0×10^{10}/s		
200	4.177	0.100	91.035
300	3.734	0.134	78.669
400	3.599	0.089	72.781
500	3.356	0.134	55.964
	Strain rate 1.0×10^{11}/s		
200	4.818	0.146	108.688
300	4.247	0.146	88.999
400	4.244	0.133	85.013
500	3.672	0.156	67.980

Compression

Tables 6, 7 and 8 show the compressive fracture strength, fracture strain and Young's modulus of HAP along the *x*-, *y*- and *z*-directions, respectively, at different strain rates and temperatures.

Figure 8 shows the stress–strain variations in the case of uniaxially compressive strain applied along the *x*-, *y*-, and *z*-direction, respectively, at the same strain rate, but different temperatures.

Figure 9 shows the stress–strain variations in the case of uniaxially compressive strain applied along the *x*-, *y*-, and *z*-direction, respectively, at the same temperature, but different strain rates.

From Figs. 8 and 9 and Tables 6–8, the compressive fracture strength and Young's modulus of HAP were found to increase significantly with the rise in strain rate. However, the temperature had almost no influence on the compressive fracture strength and Young's modulus of HAP. Moreover, it was clear that both strain rate and temperature have almost no impact on the compressive fracture strain of HAP.

On the other hand, in Yaghmaei's [12] study, when pure HAP was compressed along the *z*-direction at a temperature of 300 K and strain rate of 1.47×10^{10}/s, Young's modulus was 185.70 GPa. When it was compressed along the *y*-direction at the same temperature and strain rate of 1.027×10^{10}/s, Young's modulus was 90.60 GPa. However, in our study, at the same temperature of 300 K and a higher strain rate of 1.0×10^{11}/s, Young's modulus was 125.802 Gpa (lower than 185.70 GPa)

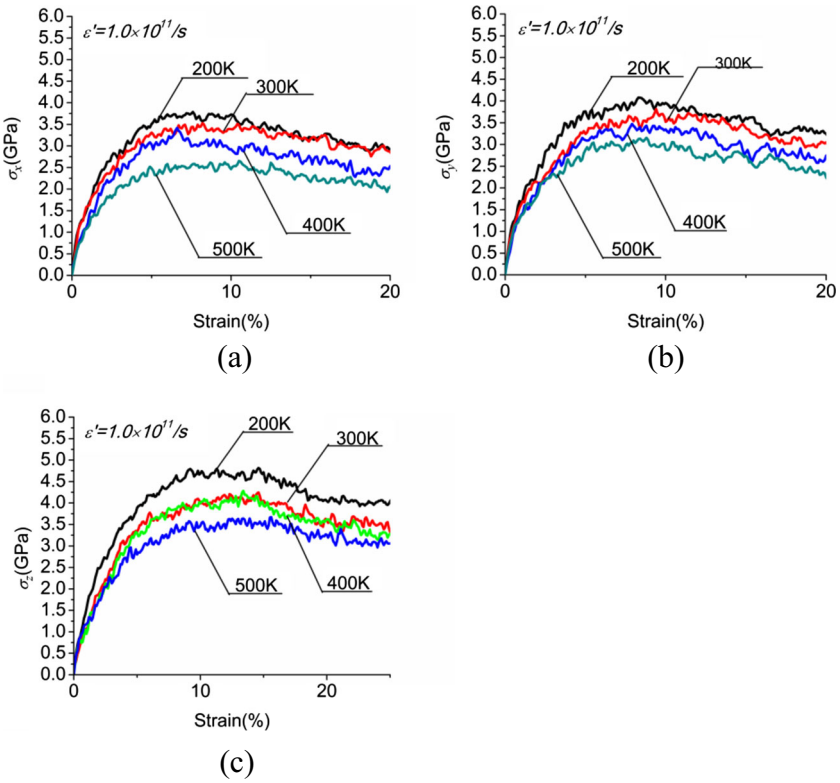

Fig. 4 Stress–strain variations for the case of uniaxially tensile strain applied along the *x*-, *y*-, *z*-direction at the same strain rate, but at different temperatures

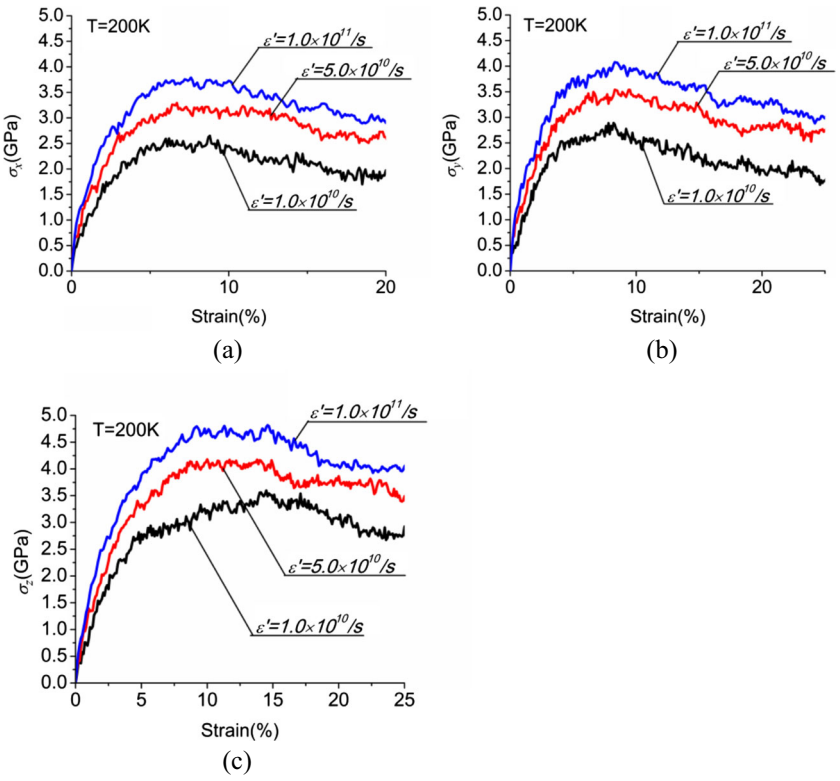

Fig. 5 Stress–strain variations for the case of uniaxially tensile strain applied along the *x*-, *y*-, *z*-direction at the same temperature, but at different strain rates

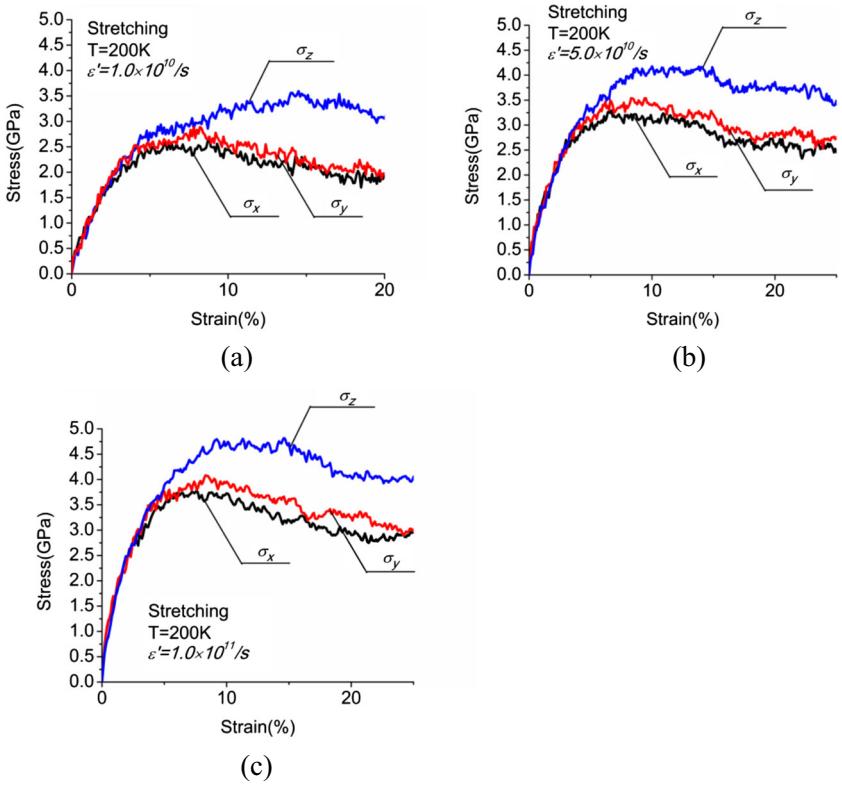

Fig. 6 Stress–strain variations for the case of uniaxially tensile strain applied along the *x*-, *y*-, and *z*-direction, respectively

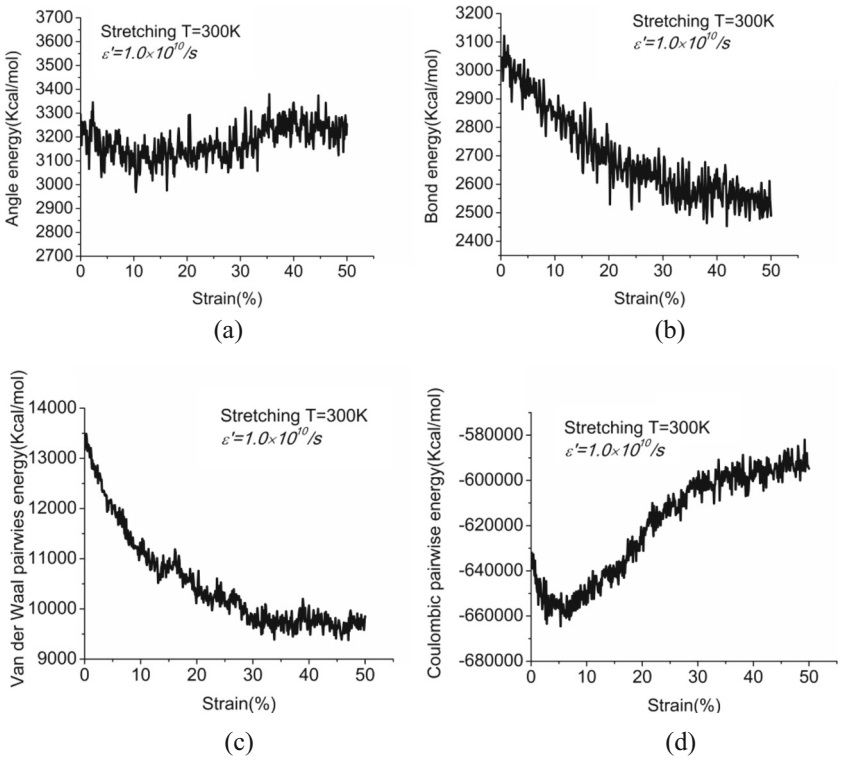

Fig. 7a–d Changes under tension in internal energy of HAP under tension at 300 K and a strain rate of 1.0×10^{10}/s. **a** Angle energy, **b** bond energy, **c** Van der Waals pairwise energy, **d** coulombic pairwise energy

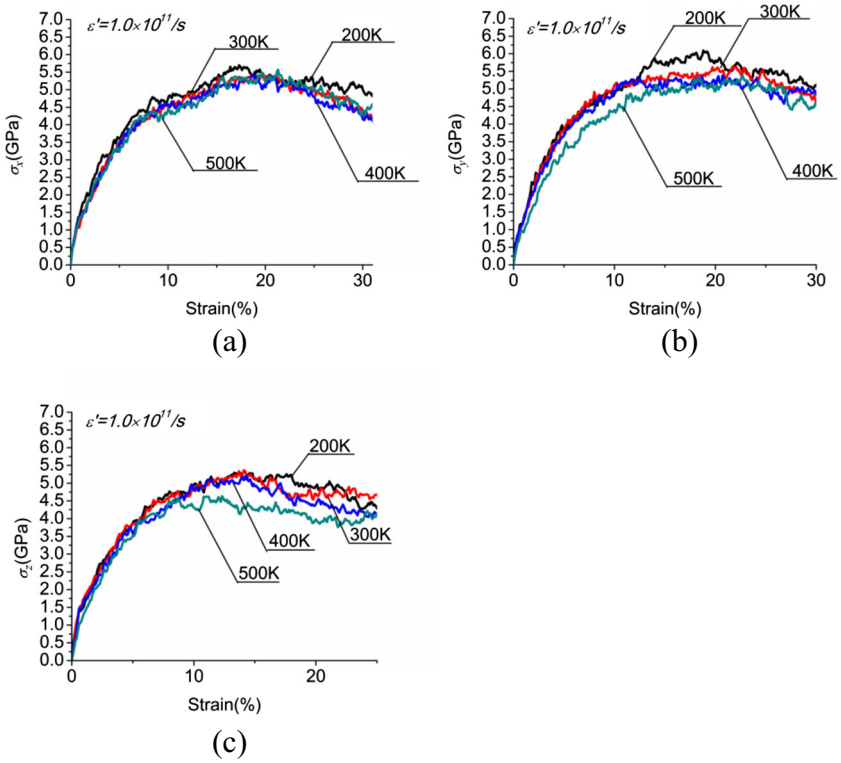

Fig. 8 Stress–strain variations in the case of uniaxially compressive strain applied along the *x*-, *y*-, and *z*-direction at the same strain rate, but different temperatures

along the *z*-direction . When the temperature was set at 300 K and a higher strain rate of 5.0×10^{10}/s was chosen, Young's modulus was 76.054 GPa (lower than 90.60 GPa) along the *y*-direction. Again, the reason for the difference is the veracity of the HAP model.

Additionally, Tables 6–8, and Fig. 10 also show that when the HAP was compressed along different directions at the same temperature and strain rate, the compressive fracture strength along the *z*-direction is always much lower than that along the *x*- and *y*-directions, and the compressive fracture

Table 6 Compressive fracture strength, fracture strain and Young's modulus of HAP along the *x*-direction in different strain rates and temperatures

Temperature (K)	Fracture strength (GPa)	Fracture strain (GPa)	Young's modulus (GPa)
	Strain rate 1.0×10^{10}/s		
200	3.791	0.192	67.053
300	3.594	0.175	61.602
400	3.132	0.153	57.021
500	3.263	0.169	58.089
	Strain rate 5.0×10^{10}/s		
200	4.765	0.166	88.420
300	4.755	0.207	76.551
400	4.246	0.168	77.913
500	4.419	0.175	79.032
	Strain rate 1.0×10^{11}/s		
200	5.698	0.173	103.694
300	5.491	0.196	93.375
400	5.439	0.186	91.412
500	5.573	0.213	94.05

Table 7 Compressive fracture strength, fracture strain and Young modulus of HAP along the *y*-direction at different strain rates and temperatures

Temperature (K)	Fracture strength (GPa)	Fracture strain (GPa)	Young's modulus (GPa)
	Strain rate 1.0×10^{10}/s		
200	3.829	0.181	67.236
300	3.484	0.160	62.306
400	3.257	0.192	69.117
500	3.018	0.136	52.330
	Strain rate 5.0×10^{10}/s		
200	4.975	0.191	82.533
300	4.771	0.206	76.054
400	4.412	0.129	74.861
500	4.187	0.025	72.708
	Strain rate 1.0×10^{11}/s		
200	6.093	0.188	104.490
300	5.634	0.217	105.715
400	5.384	0.207	99.157
500	5.380	0.227	85.596

Table 8 The compressive fracture strength, fracture strain and Young's modulus of HAP along the *z*-direction at different strain rates and temperatures

Temperature (K)	Fracture strength (GPa)	Fracture strain (GPa)	Young's modulus (GPa)
	Strain rate 1.0×10^{10}/s		
200	3.264	0.119	81.611
300	3.308	0.086	74.611
400	2.987	0.105	74.001
500	2.627	0.055	80.131
	Strain rate 5.0×10^{10}/s		
200	4.452	0.111	107.055
300	4.332	0.099	109.782
400	4.250	0.121	87.186
500	4.024	0.09	92.153
	Strain rate 1.0×10^{11}/s		
200	5.293	0.133	117.542
300	5.362	0.141	125.802
400	5.209	0.143	112.082
500	4.632	0.123	106.973

strength along the *y*-direction is a little bit higher than that along the *x*-direction. This means that the compressive property of HAP along the *x*- and *y*-directions is much better than that along the *z*-direction, and the compressive property along the *y*-direction is a little better than that along the *x*-direction. Moreover, the compressive Young's modulus of HAP along the *z*-direction (Base direction) was always found to be higher than that along the *x*- and *y*-directions (Side direction) at the same temperature and strain rate. This result meshes well with the experimental indentation data in the studies by Saber-Samandari [3] and Zamiri [4], and the nano- and microindentation experiments of Viswanath [5]. All these latter authors reported that the compressive Young's modulus along the Base (0001) direction was higher than that along the Side (1010) direction.

Figure 11 shows the change in potential energy in HAP under compression at 300 K and the strain rate of 1.0×10^{10}/s. From Fig. 11a, b, we can see that the angle energy ranges from about 3,200 kcal mol^{-1} to about 4,000 kcal mol^{-1}, and the bond energy ranges from about 2,800 kcal mol^{-1} to 3,450 kcal mol^{-1}. Both the change in bond energy and angle energy can be attributed to the change in molecular energy when HAP was under compression. Figure 11c, d demonstrates that the variation amplitude of the Van der Waals pairwise energy is very small compared with the Coulombic pairwise energy. It can therefore be considered that, during compression, the change in pair energy in pure HAP is caused mainly by the change in Van der Waals pairwise energy.

Comparing Tables 3 and 6 (*x*-direction), Tables 4 and 7 (*y*-direction), Tables 5 and 8 (*z*-direction), the compressive fracture strength and Young's modulus of HAP are always higher than the tensile fracture strength and Young's modulus. It can therefore be concluded that the compressive property of HAP is better than its tensile property.

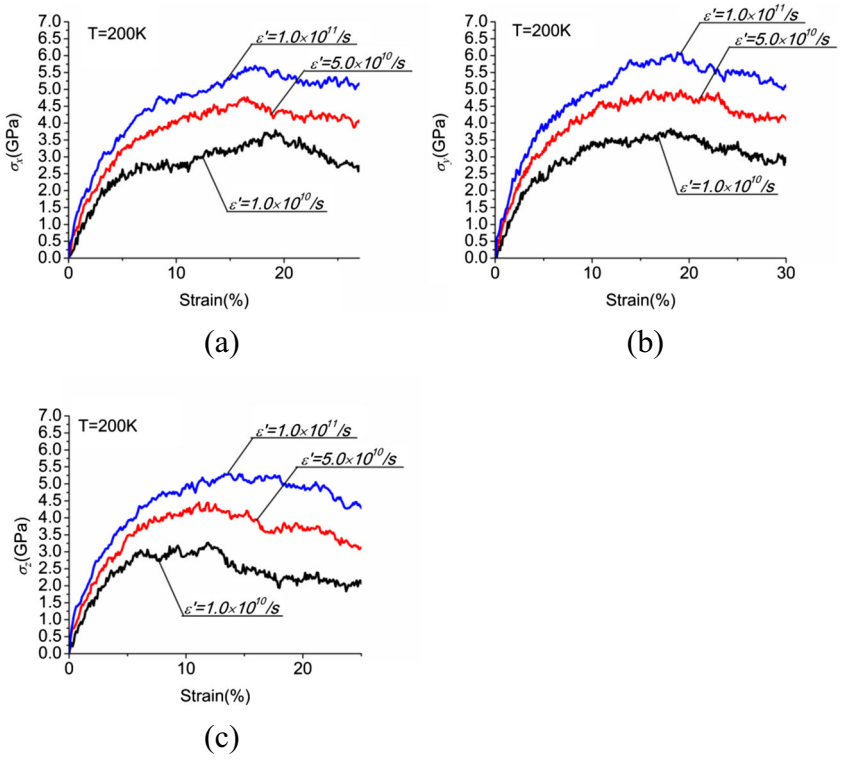

Fig. 9 Stress–strain variations in the case of uniaxially compressive strain applied along the *x*-, *y*-, and *z*-direction at the same temperature, but at different strain rates

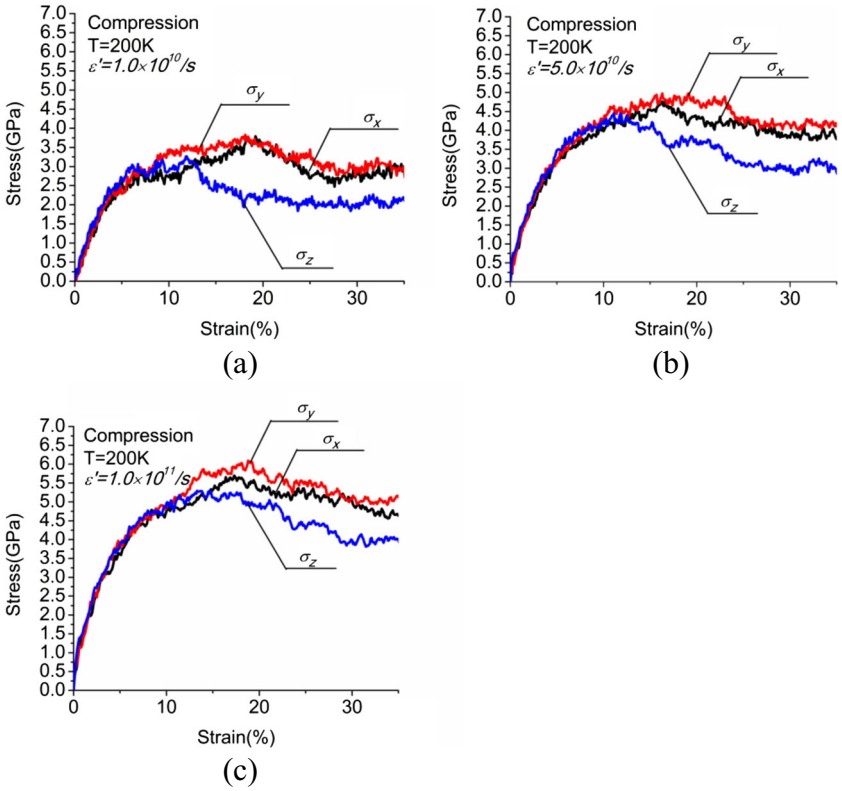

Fig. 10 Stress–strain variations in the case of uniaxially compressive strain applied along the *x*-, *y*-, and *z*-directions, respectively

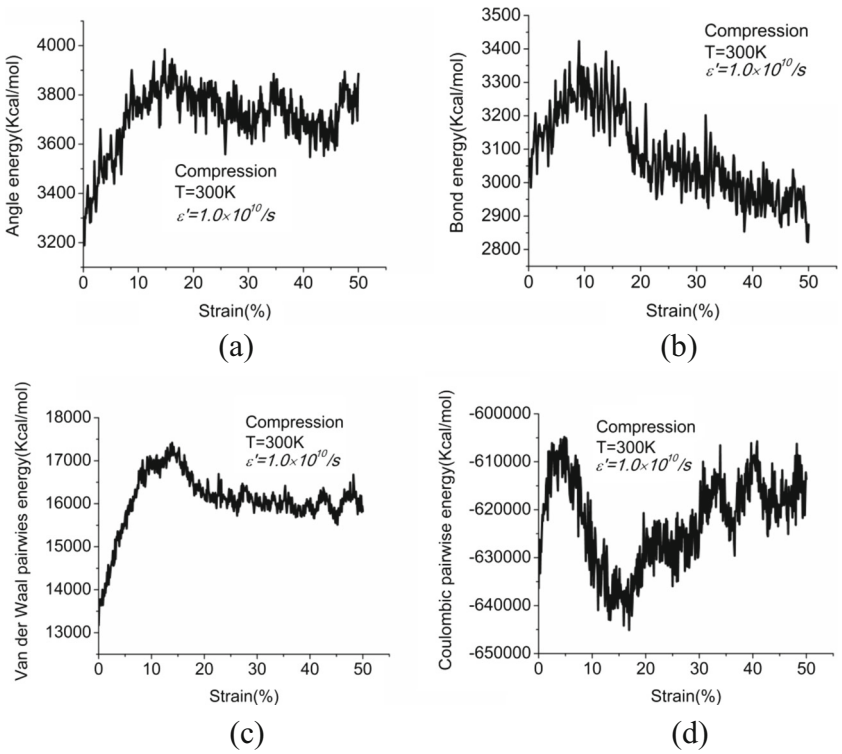

Fig. 11 Changes under compression in internal energy of HAP under compression at 300 K and a strain rate of 1.0×10^{10}/s. **a** Angle energy, **b** bond energy, **c** Van der Waals pairwise energy, **d** Coulombic pairwise energy

Conclusions

This paper demonstrates, for the first time, the result of new charges of monoclinic HAP through the QEq charge equilibration method. We modeled pure HAP in Materials Studio (http://accelrys.com/products/materials-studio/), and successfully performed MD simulations of the uniaxially tensile and compressive properties of HAP in Lammps (http://lammps.sandia.gov/). Our studies revealed that the new charges calculated through the QEq charge equilibration method make the location of the atoms in HAP consistent with their actual location, with the phosphate group keeping its normal shape. Additionally, the tensile properties of HAP along the *z*-direction were found to be better than those along the *x*- and *y*-directions; however, the compressive properties along the *z*-direction were not as good as those along *x*- and *y*-directions. Also concluded was that the compressive property of HAP is better than its tensile property.

Acknowledgment The authors wish to acknowledge the support of the National Natural Science Foundation of China (11272123), (11472108).

References

1. Misra A, Ching WY (2013) Theoretical nonlinear response of complex single crystal under multi-axial tensile loading. Sci Rep 3:1488
2. Menéndez-Proupin E, Cervantes-Rodríguez S, Osorio-Pulgar R, Franco-Cisterna M, Camacho-Montes H, Fuentes ME (2011) Computer simulation of elastic constants of hydroxyapatite and fluorapatite. J Mech Behav Biomed Mater 4(7):1011–1020
3. Saber-Samandari S, Gross KA (2009) Micromechanical properties of single crystal hydroxyapatite by nanoindentation. Acta Biomater 5(6):2206–2212
4. Zamiri A, De S (2011) Mechanical properties of hydroxyapatite single crystals from nanoindentation data. J Mech Behav Biomed Mater 4(2):146–152
5. Viswanath B, Raghavan R, Ramamurty U, Ravishankar N (2007) Mechanical properties and anisotropy in hydroxyapatite single crystals. Scr Mater 57(4):361–362
6. Elliott JC, Mackie PE, Young RA (1973) Monoclinic hydroxyapatite. Science 180(4090):1055–1057
7. Kingon AI, Maria J-P, Streiffer SK (2000) Alternative dielectrics to silicon dioxide for memory and logic devices. Nature 406(6799): 1032–1038
8. Raut VP, Agashe MA, Stuart SJ, Latour RA (2006) Molecular dynamics simulations of peptide–surface interactions. Langmuir 22(5):2402–2402
9. Martinetti R, Dolcini L, Mangano C (2005) Physical and chemical aspects of a new porous hydroxyapatite. Anal Bioanal Chem 381(3): 634–638
10. Mendez-Gonzalez M (2004) Preparation of porous hydroxyapatite tablets and porous hydroxyapatite coatings for orthopaedic use. AIP Conf Proc 724(1):262–264
11. Annie J, Liu H, Yoshito I, Yasuhiko T (2001) A trial to prepare biodegradable collagen hydroxyapatite composites for bone repair. J Biomater Sci Polym Ed 12(6):689–705
12. Yaghmaei K, Tavakoli-Darestani R, Rafii-Tabar H (2011) Molecular dynamics simulation of stress–strain relation in carbon nanotube-reinforced hydroxyapatite nanocomposite. J Comput Theor Nanosci 8(9):1870–1877
13. Maple JR, Dinur U, Hagler AT (1988) Derivation of force fields for molecular mechanics and dynamics from ab initio energy surfaces. Proc Natl Acad Sci USA 85(15):5350–5354
14. Rappé AK, Goddard WA (1991) Charge equilibration for molecular dynamics simulations. J Phys Chem 95(8):3358–3363
15. Ennari J, Sundholm F, Hamara J (1997) Vibrational spectra as experimental probes for molecular models of ion-conducting polyether systems. Polymer 38(15):3733–3744
16. Maple JR, Hwang M-J, Stockfisch TP, Dinur U, Waldman M, Ewig CS, Hagler AT (1994) Derivation of class II force fields. I. Methodology and quantum force field for the alkyl functional group and alkane molecules. J Comput Chem 15(2):162–168
17. Sun H, Mumby SJ, Maple JR, Hagler AT (1994) An ab initio CFF93 all-atom force field for polycarbonates. J Am Chem Soc 116(7): 2978–2987
18. Sun H (1994) Force field for computation of conformational energies, structures, and vibrational frequencies of aromatic polyesters. J Comput Chem 15(7):752–768